

Stability and deformation of biomolecular condensates under the action of shear flow

Luis E Coronas, Thong Van, Antonio Iorio, Lisa J Lapidus, Michael Feig, Fabio Sterpone

▶ To cite this version:

Luis E Coronas, Thong Van, Antonio Iorio, Lisa J Lapidus, Michael Feig, et al.. Stability and deformation of biomolecular condensates under the action of shear flow. The Journal of Chemical Physics, 2024, 160 (21), pp.215101. 10.1063/5.0209119. hal-04601554

HAL Id: hal-04601554 https://hal.science/hal-04601554v1

Submitted on 5 Jun 2024

HAL is a multi-disciplinary open access archive for the deposit and dissemination of scientific research documents, whether they are published or not. The documents may come from teaching and research institutions in France or abroad, or from public or private research centers. L'archive ouverte pluridisciplinaire **HAL**, est destinée au dépôt et à la diffusion de documents scientifiques de niveau recherche, publiés ou non, émanant des établissements d'enseignement et de recherche français ou étrangers, des laboratoires publics ou privés.

Copyright

PLEASE CITE THIS ARTICLE AS DOI: 10.1063/5.0209119

Stability and deformation of biomolecular condensates under the action of shear flow

Luis E. Coronas,¹ Thong Van,² Antonio Iorio,¹ Lisa J. Lapidus,² Michael Feig,³ and Fabio Sterpone¹ Université Paris Cité, CNRS, Laboratoire de Biochimie Théorique, 13 rue Pierre et Marie Curie, 75005, Paris, France

²⁾Department of Physics and Astronomy, Michigan State University, East Lansing, Michigan 48824, United States

³⁾Department of Biochemistry and Molecular Biology, Michigan State University, East Lansing, Michigan 48824, United States

(*Electronic mail: fabio.sterpone@ibpc.fr)

(Dated: 13 May 2024)

Biomolecluar condensates play a key role in cytoplasmic compartmentalization and cell functioning. Although extensive research on the physico-chemical, thermodynamic, or crowding aspects of the formation and stabilization of the condensates, one less studied feature is the role of external perturbative fluid flow. In fact, in living cells shear stress may arise from streaming or active transport processes. Here, we investigate how biomolecular condensates are deformed under different types of shear flows. We first model Couette flow perturbations via two-way coupling between the condensate dynamics and fluid flow by deploying Lattice Boltzmann Molecular Dynamics. We then show that a simplified approach where the shear flow acts as a static perturbation (one-way coupling) reproduce the main features of the condensate deformation and dynamics as a function of the shear rate. With this approach, that can be easily implemented in molecular dynamics simulations, we analyze the behavior of biomolecular condensates described through residue-based coarse grained models, including intrinsically disordered proteins and protein/RNA mixtures. At a lower shear rate the fluid triggers the deformation of the condensate (spherical to oblated object), while at higher shear rates it becomes extremely deformed (oblated or elongated object). At very high shear rate the condensates is fragmented. We also compare how condensates of different sizes and composition respond to shear perturbation, and how their internal structure is altered by external flow. Finally, we consider the Poiseuille flow that realistically models the behavior in microfluidic devices in order to suggest potential experimental designs for investigating fluid perturbations in vitro.

I. INTRODUCTION

Membraneless organelles, such as P-bodies, germ granules, and stress granules play an essential role in cytoplasmic compartmentalization and cell survival¹. For example, they regulate the cellular response to stress conditions such as starvation² or heat³, control the DNA damage response⁴, and constitute a cytoprotective mechanism against the formation of toxic aggregates⁵. They are formed upon liquid-liquid phase separation (LLPS) resulting in micron-size biomolecular condensates that exhibit liquid-like behavior^{6–8}.

Despite extensive experimental and computational research on the physico-chemical conditions that drive LLPS, one less studied feature is the possible role of perturbative fluid flow. In cellular cytoplasms, streaming and transport processes occur as an effect of internal forces associated with molecular motors, remodelling of the cyto-skeleton and motions of the cells ^{9,10}. The resulting flow currents impact the diffusion of macromolecules in the cytoplasm as well as the localization of organelles. In internodal cells of Chara corallina, the opposite motions of myosins generates a shear flow rate of $\dot{\gamma} \sim 10 \, \mathrm{s}^{-111}$. In human neurons, slow axonal transport of nonmembranous cargoes generates shear rates at the order of $\dot{\gamma} \sim 10^{-2} - 10^{-1} \text{ s}^{-112-14}$, whereas fast axonal transport of mitochondria and Golgi-derived vesicles reaches shear rates of $\dot{\gamma} \sim 6 - 40 \text{ s}^{-113-16}$. It was proposed that the streaming in the cytoplasmic environment may impact the structure and internal organization of condensates. For example, it was reported that because of their liquid state, ribonucleoprotein granules

are deformed in neuronal axons when streamed at velocities greater than $3\,\mu\text{m/s}^{17}$. In an experimental study, it was also shown that condensates of FUS deform and elongate to create fibers when exposed to shear flow of rate $\dot{\gamma} \sim 10^2 - 10^3 \, \text{s}^{-114}$.

In this work, we study how shear stress (Couette and Poiseuille flows) affects the structure and stability of biomolecular condensates. For this purpose, we employ the Lattice-Boltzmann Molecular Dynamics (LBMD) technique. LBMD accounts for hydrodynamic interactions (HI), including both the protein response due to the action of the fluid, and the perturbation on the fluid stream due to the presence of the protein (two-way coupling). However, the detailed twoway coupling may not be required to account for the deformation or stability limit under shear stress. Moreover, the explicit calculation of HI via the Lattice-Boltzmann formalism limits the length and timescales that can be accessed via simulation in current implementations of LBMD. To overcome these constraints, we tested the static velocity gradient (SVG) approach as a simplified model for the fluid. SVG describes the fluid as an unperturbed external velocity profile, i. e. it neglects the perturbation on the fluid due to the presence of the proteins (one-way coupling). The benefit of this approach is that can be easily implemented in standard engines for molecular dynamics simulation. Our results show that one-way coupling simulations can capture the main features of the deformation of the condensates upon increasing shear stress. Within this framework, we systematically compare two residue-based coarse-grained protein models: OPEP v7, developed for crowded protein systems (including in-

PLEASE CITE THIS ARTICLE AS DOI: 10.1063/5.0209119

trinsically disordered proteins)¹⁸, and COCOMO, developed specifically to describe concentration-dependent phase separation processes involving proteins and RNA polymers ¹⁹. Finally, we analyze the perturbation on the condensate produced by Poiseuille flow, mimicking the flow produced in microfluidic experimental devices¹⁴. Our work provides a detailed characterization of biomolecular condensate models in the presence of biologically relevant shear flows. The results furthermore define parameters for designing future experiments to study the deformation of biomolecular condensates under perturbative fluid flow.

II. MODEL AND METHODS

A. OPEP and COCOMO residue-based models

In this work, we describe the biomolecular condensates though OPEP v7¹⁸ and COCOMO¹⁹ coarse-grained force fields. In both models, protein residues are represented as a single interacting bead with chemical specificity and solvent effects are captured only implicitly.

The model OPEP v7²⁰ has been recently parameterized to describe crowded solutions of proteins where protein structures are maintained via elastic networks^{18,20–22}. The model has also been tested and tuned for intrinsic disordered proteins (IDPs), eg. modelling amyloid aggregations^{5,23}. For IDPs, the interaction potential includes bonded (harmonic and angle potentials) and non bonded interactions. The latter are described by pair-wise short-range potentials that are either purely repulsive or attractive-repulsive, reflecting the screening from ions in cytoplasmic environments¹⁸. OPEP v7 does not include explicit electrostatic interactions.

COCOMO was recently developed to model LLPS in protein and protein/RNA mixtures 19 . The model represents protein amino acids and RNA nucleotides at single-bead resolution. It includes bonded (harmonic and angle terms), shortrange (van der Waals and cation- π interactions), and electrostatics via a Debye-Hückel term that represents screened electrostatic interactions. It is able to reproduce the experimental radius of gyration R_G of protein peptides, as well as the dependence of physical properties of short RNA sequence on salt concentration. COCOMO has been shown to capture the concentration dependence of LLPS for more systems than other models that have been developed recently $^{24-26}$ and it has been applied successfully to predict length-dependent LLPS involving peptides and RNA as confirmed by experiments 27 .

B. Lattice Bolzmann Molecular Dynamics (LBMD) method: two-way coupling

The presence and motion of biological systems, typically solvated in an aqueuous environment, perturb the surrounding fluid particles and modify the streaming velocity field. In turn, collisions between fluid particles and protein atoms also have an impact in the motion and conformation of biological systems. The LBMD method^{28,29} aims to incorporate such

hydrodynamic interactions (two-way coupling) in simulations with implicit solvent models. The computation of hydrodynamic interactions is based on a discretization of the fluid volume onto a regular grid. In each grid site, the fluid is represented through the probability distribution of the number of fluid particles having a discrete speed $f_p(\mathbf{x},t)$, where p indicates a discrete velocity vector. The time evolution of $f_p(\mathbf{x},t)$ is given by²⁹

$$f_p(\mathbf{x} + \mathbf{c}_p \Delta t, t + \Delta t) =$$

$$f_p(\mathbf{x}, t) - \omega \Delta t \left(f_p(\mathbf{x}, t) - f_p^{\text{eq}}(\mathbf{x}, t) \right) + g_p(\mathbf{x}, t),$$
(1)

where \mathbf{c}_p is the velocity in direction p and ω is the relaxation frequency, related to the fluid kinematic viscosity. Equation (1) accounts for molecular collisions relaxing the fluid towards the Maxwellian equilibrium distribution $f_p^{\mathrm{eq}}(\mathbf{x},t)$ according to the BGK (Bhatnagar-Gross-Krook) collisional operator. The term $(g_p(\mathbf{x},t))$ accounts for the external forcing due to the momentum exchange with the particles motion, see Refs for a detailed formulation 29,30 . The action of the fluid on the particle motion is accounted by a drag force, $\mathbf{f}_i^D = -\zeta m_i(\mathbf{v}_i - \tilde{\mathbf{u}}(r_i))$ where ζ is the friction coefficient, \mathbf{v}_i is the velocity of particle i and $\tilde{\mathbf{u}}(r_i)$ is the fluid velocity at the particle position. The parameter ζ can be tuned for each system in order to match the resulting diffusivity of the molecular species to a given reference value.

The LBMD method has been implemented in the in-house Muphy software^{29,31}. The method has been applied in a number of cases, including amyloid aggregation, in absence of shear^{32,33} and with shear²³, crowded protein solutions^{5,21,22}, protein unfolding under Couette flow^{34,35}, and also for flow processes beyond the molecular scale³⁶.

C. Static Velocity Gradient (SVG) method: one-way coupling

An explicit account of hydrodynamic interactions with two-way coupling is necessary to reproduce water-mediated interactions between spatially separated clusters of biomolecules. However, a simpler description of the fluid, at reduced computational cost, might be sufficient to study the deformation and structural reorganization of biomolecular condensates under shear flow. In fact, the cost for the LB integration amount to about 40% up to 70% of the total cost of a LBMD simulations of a condensate, depending on the grid resolution, and the ratio among the number of particles and grid points. We propose here the Static Velocity Gradient (SVG) method that is validated by comparison with full LBMD simulations.

The SVG method describes the fluid as an unperturbed external velocity field $\mathbf{v}^{\text{fluid}}(\mathbf{x})$ that pushes the protein beads with a force that is proportional to $\mathbf{v}^{\text{fluid}}$ at the position of the bead \mathbf{x}_i . In SVG simulations, the evolution of the system is given by a modified Langevin equation

$$m_i \frac{d\mathbf{v}_i}{dt} = \mathbf{f}_i + \mathbf{f}^{\text{fluid}}(\mathbf{x}_i) - \zeta m_i \mathbf{v}_i + \mathbf{R}_i,$$
 (2)

This is the author's peer reviewed, accepted manuscript. However, the online version of record will be different from this version once it has been copyedited and typeset PLEASE CITE THIS ARTICLE AS DOI: 10.1063/5.0209119

tions given by the force field (either OPEP v7 or COCOMO), \mathbf{R}_i is the thermal noise, and ζ is the friction coefficient. At variance with classical Langevin dynamics, we include an external non-conservative force $\mathbf{f}^{\text{fluid}} = \zeta m_i \mathbf{v}^{\text{fluid}}(\mathbf{x}_i)$ accounting for the force acting on the system due to the presence of the fluid. The use of the Langevin friction coefficient ζ as the proportionality factor between $\mathbf{f}^{\text{fluid}}$ and $\mathbf{v}^{\text{fluid}}$ ensures that the external fluid term in Equation (2) is correctly balanced with respect to the other terms in the equation, i. e., they are expressed in the same units. We integrate Equation (2) using the leap-frog algorithm³⁷, considering the addition of \mathbf{f}_i and $\mathbf{f}^{\text{fluid}}(\mathbf{x}_i)$ as a single force term (Supplementary Information (SI), see Supplementary Text). It is worth noting that classical Langevin dynamics is recovered if $\mathbf{v}^{\text{fluid}} = 0$. In this work, we consider Couette and Poiseuille shear flows. The reader can find details on these two types of flow in Ref. ³⁸. The Couette flow results from the tangential motion of two parallel planes, or by the rotation of two coaxial cylinders at different angular velocity³⁹. Here, we assume two parallel Z planes that move at the same speed v^{max} but in opposite X direction. If the distance between the Z planes is h, then the velocity field of the fluid is

where m_i is the mass of the *i*-th protein bead and \mathbf{v}_i its ve-

locity, $\mathbf{f}_i = -\nabla U(\mathbf{X})$ is the force resulting from the interac-

 $\mathbf{v}^{\text{Couette}} \equiv \dot{\gamma}(z-z_0)\mathbf{u}_{\mathbf{x}},$

(3)

where $\dot{\gamma} \equiv 2v^{\text{max}}/h$ is the shear rate, z_0 is the Z coordinate of the center of the channel, and $\mathbf{u}_{\mathbf{x}}$ is the unit vector along the X axis. Hence, the velocity of the fluid at the center of the channel is zero and increases linearly with z.

The Poiseuille flow is produced by a constant pressure difference between two parallel planes³⁸. If the flow channel has a rectangular shape, the velocity profile is parabolic, being maximum at the center of the channel. Here we assume that the fluid is confined between two parallel Z walls at distance h, and that the pressure difference is applied along the X direction. Then the velocity profile is

$$\mathbf{v}^{\text{Poiseuille}} \equiv \left[-\frac{4v^{\text{max}}}{h^2} (z - z_0)^2 + v^{\text{max}} \right] \mathbf{u_x}. \tag{4}$$

We implemented SVG in OpenMM 7.7.0⁴⁰ as a custom Langevin integrator (SI, see Supplementary Text). This highly customizable software efficiently performs molecular dynamics simulations on graphical processing units (GPUs).

D. Simulation protocol

As a model system, we considered a condensate of the RGG intrinsically disordered domain of Laf1 proteins (Laf1-RGG, 168 residues). The initial configuration was obtained from an equilibrated COCOMO simulation ¹⁹, by discarding the dilute phase and then selecting a portion of the condensed phase with spherical shape.

We first performed a set of LBMD long simulations (500 ns) of Laf1-RGG condensate modelled with the OPEP v7 at 298 K, where we scanned different values of Couette flow shear rates. We set the friction coefficient $\zeta = 10 \text{ ps}^{-1}$ and $\Delta t = 20$ fs, to ensure the numerical stability of LBMD simulations with the OPEP v7 model¹⁸.

The size of the simulation box is 50 nm in all directions. We use a Lattice Bolzmann grid resolution of $\Delta x = 5 \text{ Å}$, resulting in 10⁶ grid points. This choice ensures that the box is large enough to accommodate condensate deformation without interacting periodic replicates, while limiting expensive computational costs due to the Lattice Boltzmann component. The system was confined in Z, whereas periodic boundary conditions apply in X and Y directions.

To validate the one-way coupling approximation, we performed simulations of Laf1-RGG condensates that mimic the conditions of those carried out with two-way coupling. In particular, we considered the Laf1-RGG condensate modeled with OPEP v7, keeping the same temperature and values of ζ and Δt , and scanned again over different Couette flow shear rates. At variance with two-way coupling, in one-way coupling simulations the size of the simulation box has no impact on the performance. Here we consider a simulation box of 150 nm in X and Y directions (periodic), and 106 nm in Z (confined).

After validation, we applied the same one-way coupling simulation protocol using COCOMO and OPEP v7 models in a more systematic analysis of different shear rates, system sizes, and a condensate with a different molecular composition. In all simulations, the temperature is 298 K and the minimum simulation time was 2 μ s, although this time was extended if the stationary regime for the condensate deformation was not reached. We stored the configuration of the system every 0.5 ns for analysis.

RESULTS AND DISCUSSION

A. Validation of one-way coupling method

We simulated the behavior of a Laf1-RGG condensate in the presence of Couette shear flow by both two-way and oneway coupling methods, see Figure 1. To describe the deformation of the condensate, we considered the shape anisotropy κ^2 , a dimensionless quantity with values between 0 and 1 (Figure 1 B). In the limiting case $\kappa^2 = 0$, the protein beads forming the condensate are distributed in a perfect spherical volume, whereas $\kappa^2 = 1$ would indicate that protein beads are distributed along a line (maximum elongation). Our results show that both simulation methods exhibited the same behavior semi-quantitatively, with two transitions at increasing shear rates $\dot{\gamma}$ (Figure 1 D). First, there is a critical shear rate that triggers a deformation from spherical to oblate condensates, with $\kappa^2 \sim 0.1$. This is observed at $\dot{\gamma}_{s\to o} = 10^7 \text{ s}^{-1}$ in two-way coupling simulations. Then, with increasing shear rates, there is a second critical value at which the system becomes extremely deformed from oblate to more elongated shapes, with $\kappa^2 > 0.3$. This was observed at $\dot{\gamma}_{o \to e} = 10^8 \, \mathrm{s}^{-1}$. In that case,

PLEASE CITE THIS ARTICLE AS DOI: 10.1063/5.0209119

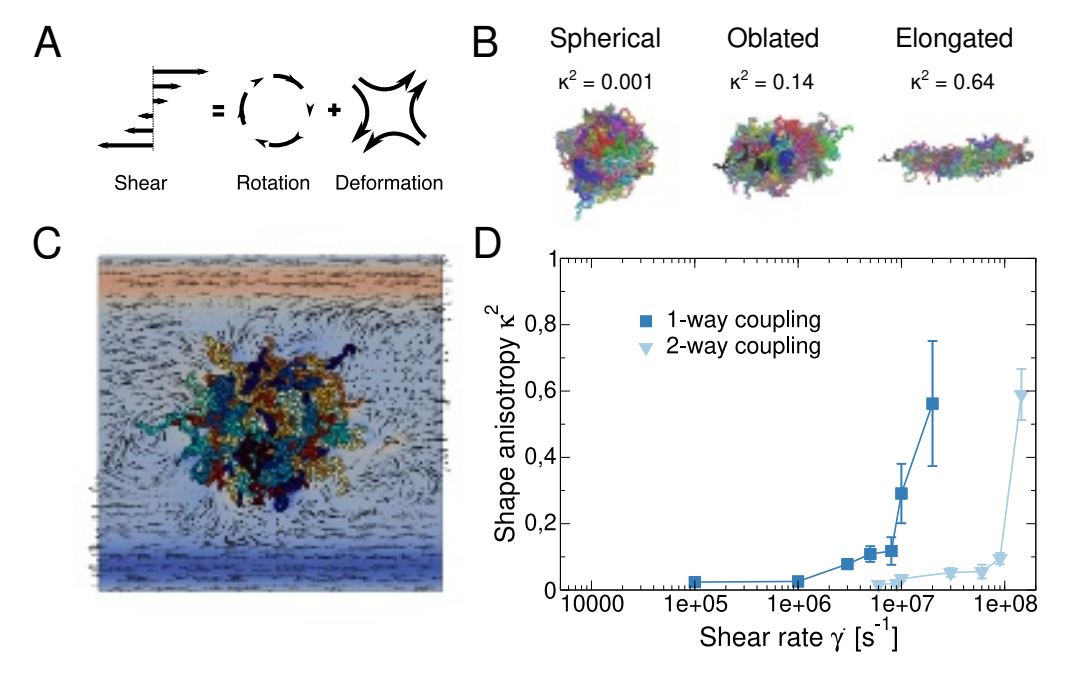


FIG. 1. A. Schematic representation of the rotational and elongational componenent of the Couette shear flow. B. Schematic representation of the possible configurations of the condensate (spherical, oblate, and elongated) and their shape anisotropy κ^2 . C. Pictorial representation of the Laf1-RGG condensate in Couette velocity field responding to the condensate motion (two-way coupling). The color background indicates the velocity gradient, and the black arrows show the instantaneous velocity field projected on the *X-Z* plane. D. Shape anisotropy for the Laf1-RGG condensate simulated at different shear flow rates using two-way (LBMD) and one-way coupling (SVG + MD). The condensate was modelled using OPEP v7 with a friction coefficient of $\zeta = 10 \text{ ps}^{-1}$.

the condensate aligned its major axis to minimize its cross section with respect to the flow. As the shear rate was increased further, the condensate was then able to keep the elongated configuration until a stability limit is reached where the condensate breaks up. This was observed at $\dot{\gamma}_{e \to b} = 2 \cdot 10^8 \text{ s}^{-1}$. With both simulation methods, the Laf1-RGG condensate could reach shape anisotropy values of up to $\kappa^2 \sim 0.6$ before breaking up. However, while there is qualitative agreement between one-way and two-way coupling simulations, all the transitions are shifted to lower shear rates by about one order of magnitude with one-way coupling vs two-way coupling. This may be expected because for one-way coupling the velocity gradient, and therefore the force applied to the condensate, is exactly determined by the shear rate. In contrast, in two-way coupling simulations the shear rate used for the analysis indicates the value in pure fluid simulations. In fact, in our simulations, the shear gradient is generated by forcing the fluid at the top and bottom extremities of the simulations box to move in opposite directions. In this manner, a velocity gradient is generated naturally in the box. In a fluid LB simulation, it is therefore possible to have a direct relationship among the amount of forcing and the shear rate generated. In LBMD, the presence of the condensate alters the velocity field of the fluid generated by the forces acting at the wall on the top and bottom of the simulation box (Figure 1C). In the vicinity of the condensate the fluid field is distorted with respect to the linear profile. This means that the effective shear rate experienced by the condensate should be lower than the shear rate generated by the same forcing in a pure fluid simulations.

However, given the qualitative agreement, the use of one-way coupling appears to be adequate for capturing the main features of physical deformation of biomolecular condensates under shear stress, but with the caveat that critical shear rates are likely underestimated by about an order or magnitude.

It is worth noting that in the two-way coupling we observe fluid reorganization (eddies) around fragments of the Lafl-RGG proteins stretching out from the condensate. These fragments work like antenna for feeling different values of the velocity gradient. This adds heterogeneity to the drag experienced by the condensate. The role of surface roughness and protrusions has been discussed for describing the response of other biomolecular systems under shear flow, e.g. the elongation/collapse of the vWf protein⁴¹, or for modelling protein unfolding⁴².

B. One-way coupling simulations of Laf1-RGG condensate

In this section, we systematically compare the behavior of Laf1-RGG condensates modeled with OPEP v7 and CO-COMO, using the computationally more efficient one-way coupling method. The aim is to generalize the finding of two transitions (spherical-oblated and oblated-elongated) previously obtained with OPEP v7 to other residue-based models.

We began by investigating the effect of the friction coefficient, ζ , on the dynamics in the dilute and condensed phases. The friction ζ is calibrated to best reproduce the diffusion

PLEASE CITE THIS ARTICLE AS DOI: 10.1063/5.0209119

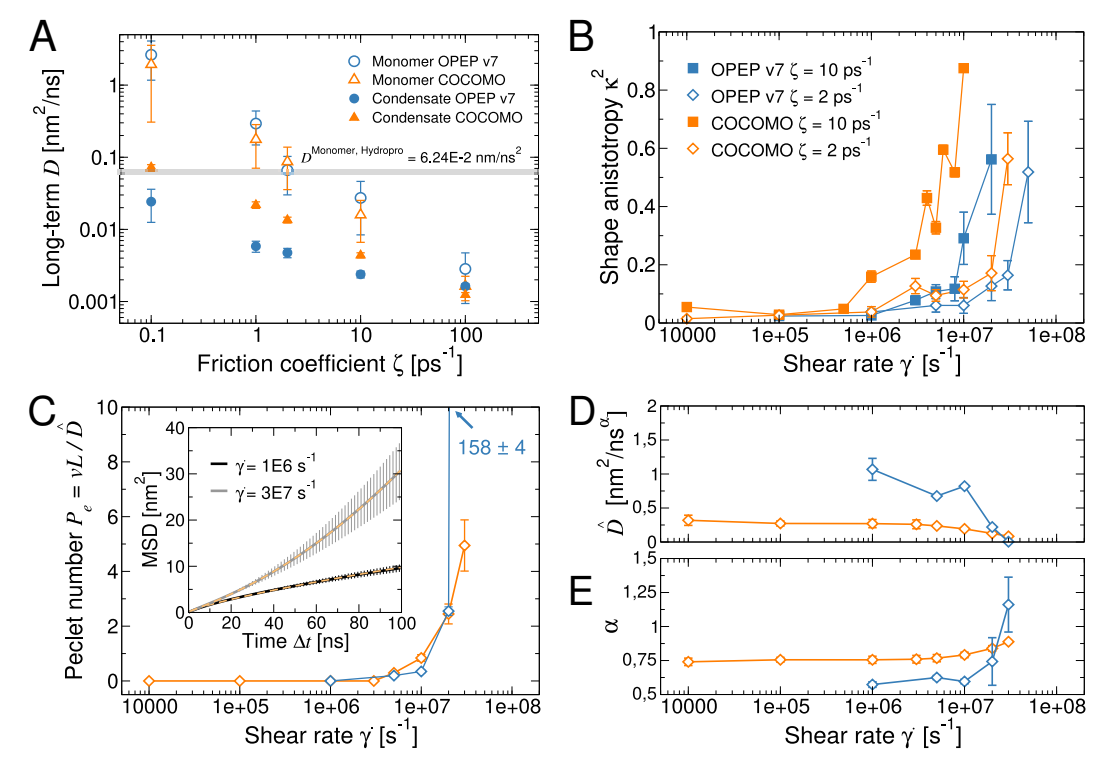


FIG. 2. Comparison between OPEP v7 (blue symbols) and COCOMO (orange symbols). A. Long-term diffusion coefficient D, in absence of shear, for Laf1-RGG monomers (open symbols) and Laf1-RGG inside a condensate (filled symbols). The black line indicates the Hydropro⁴³ prediction for the Laf1-RGG monomer under dilute conditions. Both models predict comparable diffusion for the monomers and a slowdown within the condensate. OPEP v7 predicts stiffer condensates. B: Shape anisotropy for the Laf1-RGG condensate simulated at different shear flow rates using one-way coupling and a friction coefficient of $\zeta = 10 \text{ ps}^{-1}$ (filled squares), as in the two-way coupling method, and $\zeta = 2 \text{ ps}^{-1}$ (open diamonds), the value that best fits the theoretical estimate of monomer diffusion. C. Péclet number, with friction $\zeta = 2 \text{ ps}^{-1}$. Shear rates $\dot{\gamma} \ge 10^7 \text{ s}^{-1}$ trigger the advective regime in the condensate $(P_e > 0)$. Inset: Mean-squared displacement for COCOMO Laf1-RGG inside the condensate under shear rates $\dot{\gamma} = 10^6 \, \mathrm{s}^{-1}$ (black) and $\dot{\gamma} = 5 \cdot 10^6 \, \mathrm{s}^{-1}$ (gray). Dashed lines are fit to Equation (5), we plot the Generalized diffusion coefficient \hat{D} in panel D and the diffusive exponent α in panel E.

coefficient of Laf1-RGG monomers in the dilute phase (D₀). More precisely, we calculated the mean square displacement $MSD(\Delta t)$ in the range 40 ns $\leq \Delta t \leq 100$ ns and fit the data to a linear function: $MSD(\Delta t) = 6D\Delta t + MSD_0$. Even although MSD(0) = 0, the offset MSD_0 is needed when fitting only part of the mean square displacement curve due to anomalous behavior at shorter time scales. The resulting diffusion coefficients for the monomers are similar between OPEP v7 and COCOMO across the entire range of ζ values simulated here (Figure 2A). At $\zeta = 2 \text{ ps}^{-1}$, the calculated diffusion values match the theoretical value estimated for Laf1-RGG monomers with Hydropro⁴³. Therefore, we used $\zeta = 2 \text{ ps}^{-1}$ in the one-way coupling simulations going forward unless specified otherwise.

Calculated diffusion rates of Laf1-RGG inside the condensate show that there is a slowdown of the dynamics compared with dilute conditions (Figure 2 A). Here, we removed the translation of the center of mass of the condensate before estimating the MSD. For $\zeta = 2 \text{ ps}^{-1}$, the ratio D/D_0 is about 0.07 for OPEP v7 and 0.16 for COCOMO. A ten-fold slowdown in diffusion is generally expected for highly concentrated biomolecules in liquid systems⁴⁴. The difference between the two coarse-grained models arises from a different nature of non-bonded interactions, where effective intermolecular interactions in OPEP v7 are stronger, leading to stiffer and more viscous condensates than with COCOMO. We compare the energy scale of interactions between typical amino-acid pairs in SI, Figure S1.

Next, we simulated the deformation of the condensate using OPEP v7 and COCOMO under Couette flow (Figure 2 B) using one-way coupling. To clearly show the effect of the friction coefficient, we also simulated the systems with $\zeta = 10 \, \mathrm{ps^{-1}}$. In all cases, we found the same sphere-oblate and oblate-elongated shape transitions, but the critical shear rates $\dot{\gamma}$ were shifted by approximately one order of magnitude for both OPEP v7 and COCOMO simulations when $\zeta = 10 \text{ ps}^{-1}$. This was due to the fact that ζ controls the magnitude of the drag force exerted by the fluid velocity on the molecules.

We then analyzed how Couette flow affects the diffusion of Laf1-RGG monomers inside the condensate. Following previous work, we expected that confinement of the monomers, due to crowding and containment within the condensate, results not just in a slow-down of diffusion but also anomalous (subdiffusive) behavior⁴⁵. In addition, shear induces a rigid-body rotational component to the overall condensate (Figure 1A)

PLEASE CITE THIS ARTICLE AS DOI: 10.1063/5.0209119

and couples with diffusion of individual molecules inside the condensate via advection. In other works, researchers discussed how rigid-body rotation can be removed before estimating the MSD^{46,47}. Here, we are interested in keeping the advective component since it results from shear flow. Furthermore, due to the liquid-like nature of biomolecular condensates, there is no specific reference configuration that is needed for removing rotation. Finally, in absence of shear the characteristic time of the Laf1-RGG condensate rotation is of two orders of magnitude larger than the characteristic time for translation (SI, see Supplementary Text). For these reasons, we calculated the MSD after removing only the translation of the center of mass of the condensate and fitted the values to

$$MSD(\Delta t) = 6\hat{D}\Delta t^{\alpha} + v^{2}(\Delta t)^{2}, \tag{5}$$

where α is the power law exponent of the diffusive component ($\alpha=1$ normal diffusion, $\alpha<1$ subdiffusive regime, and $\alpha>1$ superdiffusive regime), \hat{D} is the generalized diffusion coefficient (\hat{D} is the usual diffusion coefficient D if $\alpha=1$), and v is the advective velocity. Since we are explicitly considering anomalous diffusion in this case, we fitted MSD within the range of $0 \leq \Delta t \leq 100$ ns (Figure 2 C, inset). The fitted values of α , \hat{D} and v^2 are reported in SI, Table S1.

Our results show the presence of subdiffusion of Laf1-RGG molecules inside the condensate over the entire range of simulated shear rates. At low $\dot{\gamma}$, where spherical and oblate condensates are present, α remains approximately constant at $\simeq 0.75 \pm 0.03$ for COCOMO and at $\simeq 0.60 \pm 0.02$ for OPEP v7. With increasing shear rates, α increases towards 1, concomitant with a sharp decrease of \hat{D} (Figure 2 D, E, SI Table S1).

To evaluate whether diffusion or advection dominates in determining Laf1-RGG dynamics inside the condensate, we calculated the Péclet number $Pe \equiv vL/\hat{D}$, where L is a characteristic length of the system. Here we set L = 10 nm. Since we are only interested in distinguishing between cases where advection is relevant, i.e. Pe> 0, and where it is not, i.e. Pe \simeq 0, the choice of L defines the unit scale of Pe but has no relevance in the results. With increasing shear rate we find a transition from subdiffusive Pe ≥ 0 to the advectivediffusive regime Pe> 0 that follows the increase in α . In both CO-COMO and OPEP v7 models this transition occurs at $\dot{\gamma} = 10^7 \text{ s}^{-1}$, approximately the same shear rate as the oblate-elongated shape transition (see Figure 2 C, SI Table S1). Once that shear rate is reached, advection dominates. However, in the COCOMO simulations the effect of advection increases more slowly. This again reflects differences in internal viscosity of the condensate, with OPEP v7 predicting a more viscous condensate (Figure 2A).

Having described the global changes of the condensate shape under shear stress we now focus on its internal structure. To this aim we separately consider spherical, oblate, and elongated condensates (Figure 3 A). For the elongated condensates, we constrain our analysis to trajectory snapshots before the rupture of the condensate.

First, we estimated the probability distribution of the end-to-end distance d_{e-e} in Laf1-RGG molecules. There is little difference between spherical and oblate condensates, but in both COCOMO and OPEP v7 simulations, we observe a shift to longer distances when condensates are elongated (Figure 3B, and SI, Figure S2, for the OPEP v7 case). This observation of shear-induced stretching resembles the formation of fibers in biomolecular condensates under shear

stress, prior to a liquid-solid transition, as reported in microfluidic experiments 14 .

Second, we analyzed inter-chain contacts. We define that two residues of different chains are in contact if their distance is less than 9 Å, shorter than the short-range interaction cutoff. Laf1-RGG molecules formed extensive contacts, more with OPEP v7 than with COCOMO (see SI, Table S2). In spherical condensates, there are 8.2 % more contacts with OPEP v7 than with COCOMO. This reflects differences in the strength of intermolecular interactions. There is no significant difference between oblate and spherical condensates. However, we observe a significant loss of internal contacts when the condensate is elongated. Compared with spherical condensates, COCOMO predicts a loss of 7.1 % contacts per molecule, while OPEP v7 predicts a loss of 4.5 % contacts.

Shear stress has an effect not only in the absolute number of contacts, but also on how they are distributed along the chains (see Figure 3). For COCOMO, we observe that head-to-tail contacts are enhanced for oblate and elongated condensates relative to spherical condensates whereas the terminal residues appear to detach, especially in elongated condensates. For OPEP v7 we did not identify a clear pattern (see SI, Figure S3).

C. Simulations of other protein and protein-RNA condensates and size effects

Since COCOMO is transferable to other systems, including systems containing RNA, we generalized the previous results to other condensing systems. First, we compared Laf1-RGG and RLP-WT condensates. Both are composed of intrinsically disordered proteins with similar length (168 and 166 residues, respectively), but different chemical composition. We equilibrated a condensate of 98 RLP-WT monomers, so that both system are of comparable size in absence of shear. Second, we considered a protein-RNA mixture composed of short peptides of 30 residues, $(RGRGG)_6$, and a homogeneous chain of 20 adenine nucleotides, A_{20} . In the equilibrated configuration of this system there is coexistence of condensed and dilute phases. However, we found that even though the mass of the condensate is not constant due to molecular exchanges between dilute and condensed phases, the fluctuations are small and do not significantly affect the estimates of the shape anisotropy of the condensate.

We found that all systems exhibited the same qualitative behavior, with critical shear rates $\dot{\gamma}_{s\to o}$ and $\dot{\gamma}_{o\to e}$ that lie between 10^6 and 10^7 s⁻¹ (see Figure 4A). It is worth noting that while the shape deformation in the shear flow was similar, the effect on the internal structure of RLP-WP was not. For example, we did not observe overall stretching of monomers as for the Laf1-RGG system, see SI Figure S2, even although we observed the same head-to-tail organization with RLP as for Laf1-RGG (see SI Figure S3).

Finally, we analyzed finite size effects on the shear-induced deformation of the condensates. We compared three RLP-WT condensates composed of 98, 180, and 720 monomers. In absence of shear, they have radii of gyration of $R_G = 8$, 10, and 15 nm. We found that with increasing size, the critical shear rates $\dot{\gamma}_{s\to o}$ and $\dot{\gamma}_{o\to e}$ decreased, making the system more sensitive to the shear flow, as shown in Figure 4B. We rationalize this behavior from the fact that the deformation is triggered by the torque generated by the force from the fluid with respect to the centroid of the condensate $\tau \equiv \mathbf{f}^{\text{fluid}} \times \mathbf{r}$. Clearly, systems of bigger size have a larger radius \mathbf{r} . Hence, equal torque on molecules near the surface of a larger condensate is generated with a weaker force $\mathbf{f}^{\text{fluid}}$ compared to smaller condensates. This is also consistent with theory describing fluid droplet deformation in shear flow⁴⁸. Another remarkable feature is that the shear threshold $\dot{\gamma}_{e\to b}$

PLEASE CITE THIS ARTICLE AS DOI: 10.1063/5.0209119

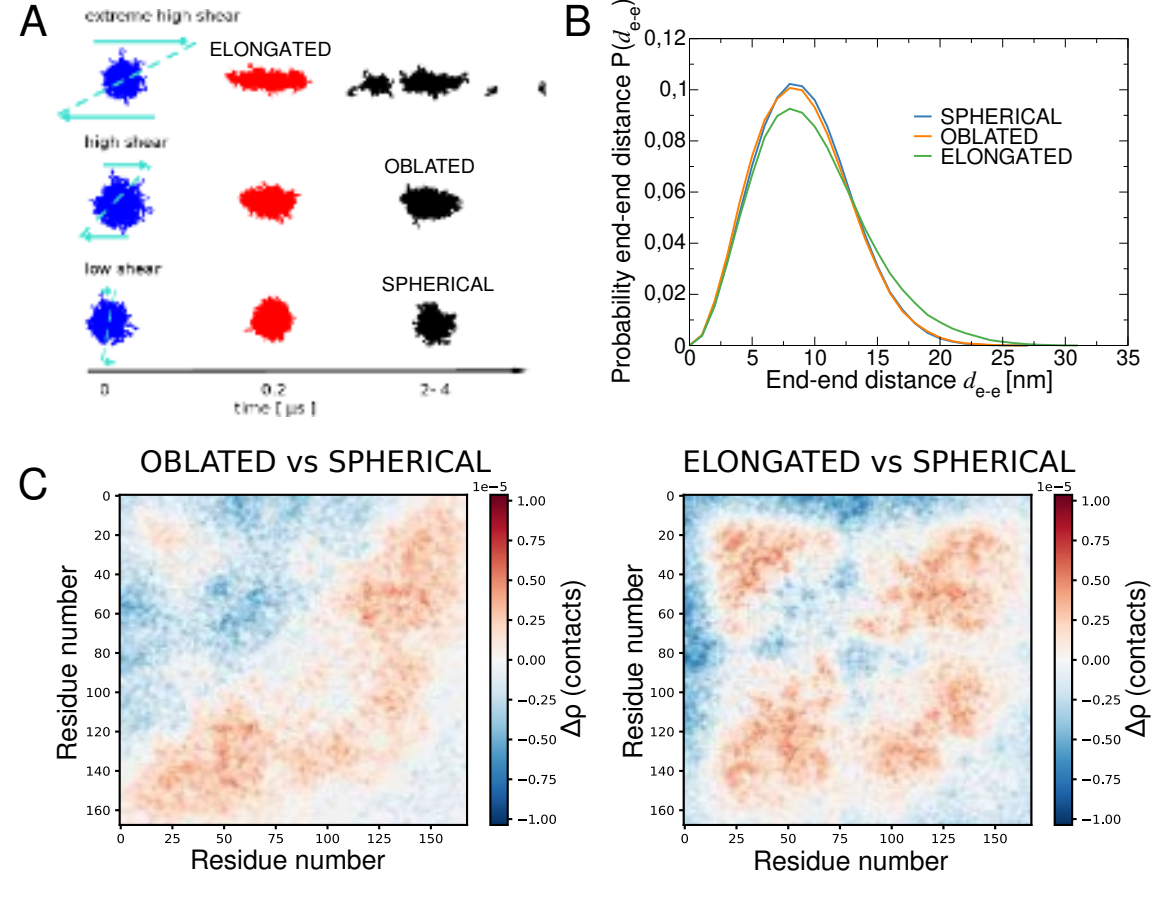


FIG. 3. Structural changes of COCOMO Laf1-RGG condensate under shear. A: schematic illustration of the condensate configuration during simulation time, for different shear rates. B: Probability distribution of the end-end distance. Extreme high shear induces stretching of the chains. C: Inter chain contact map. The absolute difference of the density of contacts $\Delta \rho$ is compared between oblate and spherical condensates (left) and between elongated and spherical condensates (right). We find that shear induces a head-to tail organization.

before condensates break up appears to be size-independent, but the largest-size condensates became extremely deformed before breaking up ($\kappa^2 \sim 0.9$). However, we note that for the largest system, the condensate may not be able to fully equilibrate within the accessible simulation times.

Extrapolation of our simulation results (in the nanometer scale) to the typical scale of in vitro experiments (micrometers 14) is not trivial. In particular, our results show a linear dependence of the critical shear rate on the droplet size, as predicted in theory 48 , but the extrapolated $\dot{\gamma}_{s\to o}$ becomes negative approaching the micrometer scale while at this scale one expects from experimental data on FUS 14 , $\dot{\gamma}_{s\to o}\sim 10^3\, s^{-1}$. We acknowledge a number of factors that may affect the finite size scaling analysis, including i) the shift of the critical shear rate between one-way and two-way coupling methods (Figure 1D); ii) how the model compares to the experimental viscosity of the condensate and slowdown of the diffusion (Figure 2A); and iii) a possible change of regime in the relationship between droplet radius and its surface tension, when the radius spans from the nanoscopic to the microscopic scale.

D. Poiseuille flow

Finally, we move our attention to the behavior of biomolecular condensates under Poiseuille flow to mimic conditions in microfluidic experimental devices. This is important for proposing potential experiments that can test the hypotheses from our simulations.

In simulations under Poiseuille flow, we considered a rectangular channel confined in the Z direction by hydrophobic attractive-repulsive walls. In this case, we started with a Laf1-RGG condensate (168 chains) in contact with the confining wall. The wall-protein bead interaction was modeled via the short-range interaction potential of alanine in COCOMO¹⁹:

$$U_{W,i} \equiv 4\varepsilon_{W,i} \left[\left(\frac{\sigma_{W,i}}{|z_i - z_W|} \right)^{10} - \left(\frac{\sigma_{W,i}}{|z_i - z_W|} \right)^5 \right], \tag{6}$$

where $\varepsilon_{W,i} = 0.4 \text{ kJ/mol}$ if the *i*-th residue is polar or 0.405 kJ/mol if it is non-polar, $\sigma_{W,i}$ ranges between 4.9 Å and 5.9 Å depending on the residue type, and $|z_i - z_W|$ is the distance to the wall.

We equilibrated the initial configuration by relaxing the condensate in contact with the wall (Figure 5A). To monitor equilibration, we calculated the contact angle θ between the condensate and the wall⁴⁹ (see SI, Figure S4 for details on its calculation) during 2 μ s

PLEASE CITE THIS ARTICLE AS DOI: 10.1063/5.0209119

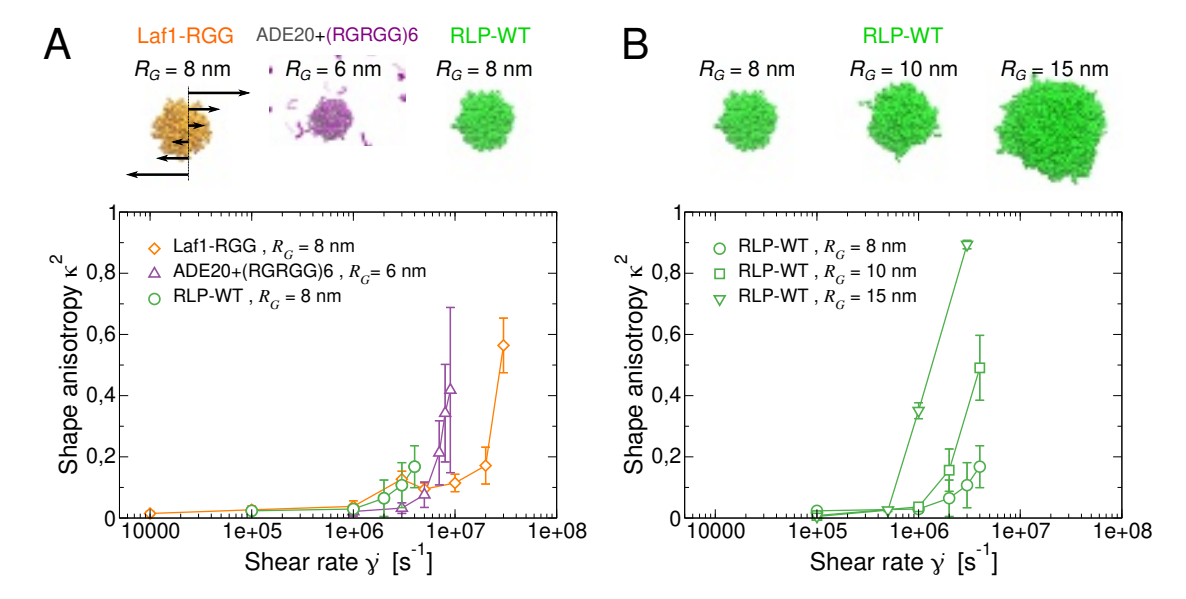


FIG. 4. A: Comparison between condensates of comparable size but with different chemical composition. Laf1-RGG and RLP-WT are composed of monomers of similar chain length (168 and 166 residues, respectively). The A₂₀/(RGRGG)₆ system is a mixture of short RNA and protein chains (20 and 30 residues respectively). B: Size effect on RLP-WT deformation under Couette flow. With increasing size, the condensates become more sensitive to the fluid force. Larger condensates are also able to keep stronger deformation before breaking.

long simulation, in the absence of shear (Figure 5B). The estimated value of θ is an important parameter when comparing simulations with experimental devices as it reflects the strength of condensate-wall interactions that can be tuned in the simulations.

Since the condensate was located close to the wall in our simulations, it was convenient to define the shear rate for Poiseuille flow as the derivative of the velocity profile at the position of the wall $\dot{\gamma} \equiv 4v^{\text{max}}/h$, see Figure 5C. A notable difference between Poiseuille and Couette flows is that in Poiseuille flow, all the fluid particles move in the same direction. As a consequence, the condensate did not remain in the center of the channel, but it was pushed along the channel in the positive X direction. Our results from simulations with one-way coupling show that there is a critical shear rate beyond which condensates were dragged away from their initial position on the wall. At that point, there was also rotation around the perpendicular Y axis (Figure 5D). At short times $\sim 0.4 \mu s$, the fluid flow had a stronger impact on the upper region of the condensate than the bottom region. As a consequence, the condensate assumed an oblique orientation with respect to the wall. In one-way coupling simulations, the condensate was under the influence of two competing forces: the attraction towards the wall and the shear force from the fluid. If the condensate-wall interaction is strong enough, the condensates adheres to the wall, minimizing its exposed cross section. However, for weaker wall interaction, the Poiseuille flow can lift the condensate towards the center of the channel.

We observed such lifting of Laf1-RGG condensates in one-way coupling when $\dot{\gamma}=8\cdot 10^6~{\rm s}^{-1}$, the highest shear rate before the condensate breaks, when COCOMO was used and wall-condensate interactions were weakened by a a factor of 10 (see SI, Figure S5). We verified that the lifting was also observed in one-way and two-way coupling simulations when using OPEP v7 for $\dot{\gamma}=10^7~{\rm s}^{-1}$ and $\dot{\gamma}=5\cdot 10^8~{\rm s}^{-1}$, respectively. For these latter cases, to adequately compare between different simulation methods, we set the friction coefficient $\zeta=10~{\rm ps}^{-1}$. The lifting is caused by the orientation taken by the condensate oblique to the flow direction which results in an effective force toward the center of the channel. This behaviour has

been extensively studied in the case of vesicles subject to Poiseuille ${\rm flow}^{50}.$

Finally, we describe the deformation of the condensate induced by the Poiseuille flow (Figure 5E). Different from the results obtained with Couette flow, we found smoother transitions from spherical to oblated and elongated condensates. As a result, shear thresholds $\dot{\gamma}_{s\to o}$ and $\dot{\gamma}_{o\to e}$ cannot be identified clearly. We hypothesize that the smoother transitions are a consequence of condensate-wall interactions. As we already mentioned, the condensate tends to adhere to the wall, giving rise to flatter configurations even without shear. Nevertheless, the range of shear rates for the deformation and breaking of the condensate are similar to what we obtained with Couette flow (i.e. 10^6 - 10^8 s⁻¹). When comparing between COCOMO and OPEP v7, we find again that with OPEP v7 deformations occurred at higher shear rates because of higher internal viscosity.

IV. CONCLUSIONS

In this work, we describe the deformation of biomolecular condensates under the influence of Couette and Poiseuille shear flow, and how it affects their stability, internal dynamics, and structural properties. We identified three steps in the deformation process under increasing shear rates. First, at low shear, we identified a sphericaloblate transition. Then, at increasing shear, the condensate elongates. Finally, for even higher shear, the condensates break. Our results indicate that this pattern is general to a wide variety of simulation setups, including Couette and Poiseuille shear flows, two different residue-based coarse grained protein models (OPEP v7 and CO-COMO), and different chemical compositions of the condensates, including intrinsically disordered proteins (Laf1-RGG, RLP-WT) and protein/RNA mixtures. With respect to diffusion of the monomers inside the Laf1-RGG condensate, our results show a shear-induced transition between subdiffusive to advective-diffusive regimes. More detailed comparisons with atomistic simulations in future work are needed to provide further insights.



the online version of record will be different from this version once it has been copyedited and typeset

PLEASE CITE THIS ARTICLE AS DOI: 10.1063/5.0209119

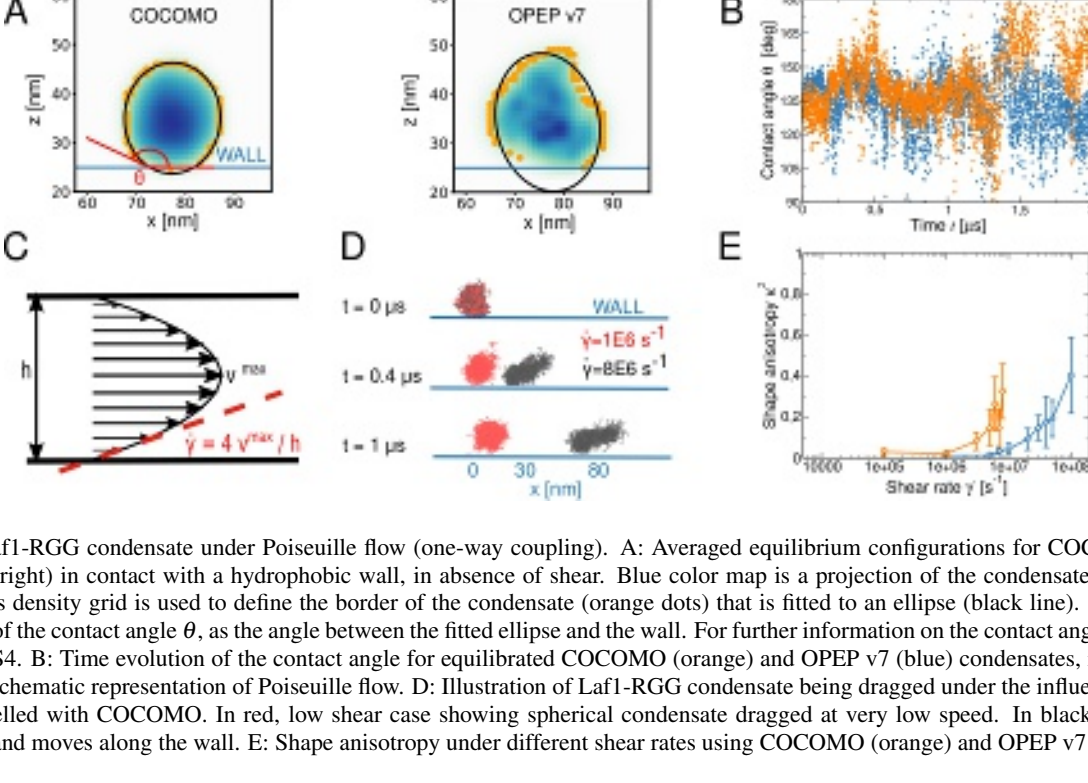


FIG. 5. Laf1-RGG condensate under Poiseuille flow (one-way coupling). A: Averaged equilibrium configurations for COCOMO (left) and OPEP v7 (right) in contact with a hydrophobic wall, in absence of shear. Blue color map is a projection of the condensate density into XZ plane. This density grid is used to define the border of the condensate (orange dots) that is fitted to an ellipse (black line). In red, graphical definition of the contact angle θ , as the angle between the fitted ellipse and the wall. For further information on the contact angle algorithm, see SI Figure S4. B: Time evolution of the contact angle for equilibrated COCOMO (orange) and OPEP v7 (blue) condensates, in the absence of shear. C: Schematic representation of Poiseuille flow. D: Illustration of Laf1-RGG condensate being dragged under the influence of Poiseuille flow, modelled with COCOMO. In red, low shear case showing spherical condensate dragged at very low speed. In black, the condensate elongates and moves along the wall. E: Shape anisotropy under different shear rates using COCOMO (orange) and OPEP v7 (blue).

From a computational point of view, we highlight the application of one-way coupling based on a static gradient to model external fluid flow for simulations of large biological systems like the condensates described here. We show that this approach maintains the key features of a more physically-realistic two-way coupling as described in LBMD simulations, but with reduced computational cost. Moreover, the one-way coupling can be easily implemented in standard codes for molecular dynamics simulations.

The simulation of condensate deformation under Poiseuille flow opens the door for future applications to design microfluidic experimental devices. This will enable combined simulation/in vitro studies of the deformation of biomolecular condensates under shear flow. Finally, we note that according to our calculation, the numerical critical shear rate ($\sim 10^6 - 10^7 \text{ s}^{-1}$) needed to deform the condensate is larger than characteristic values reported from experiments $(10^2 - 10^3 \text{ s}^{-1})$. It is expected that for a small condensate (10 nm), which can be simulated at amino-acid resolution, deformations occur at much higher shear rates than for the condensates studied in the experiments ($\sim 1 \mu m$). Bridging the gap in scale between simulations and experiment to better understand the size-effect on critical shear rates remains a challenge that will require further methodological innovations, like the application of two-phase lattice Boltzmann.

SUPPLEMENTARY INFORMATION

The Supplementary Information file contains:

- · Supplementary Text
 - Custom Langevin inregrator in OpenMM (SVG method).
 - Translational and rotational diffusion in absence of shear.

- Tables S1-S2
- Figures S1-S5.

ACKNOWLEDGMENTS

LC, AI and FS acknowledge the financial support by the "Initiative d'Excellence" program from the French State (Grant "DYNAMO", ANR-11-LABX-0011-01, and "CACSICE", ANR-11-EQPX-0008). FS. LC acknowledge support from Grant "CondFlow" ANR-22-CE95-0002. MF, LL, and TV acknowledge support from the US National Science Foundation under grant MCB 2210228. Part of this work was performed using HPC resources from GENCI [CINES, TGCC, IDRIS] (grant x20236818) and LBT.

AUTHOR DECLARATION

The authors have no conflicts to disclose.

DATA AVAILABILITY

The data that support the findings of this study are available from the corresponding author upon reasonable request.

¹S. F. Banani, H. O. Lee, A. A. Hyman, and M. K. Rosen, Nature Reviews Molecular Cell Biology 18, 285 (2017).

²W. van Leeuwen and C. Rabouille, Traffic **20**, 623 (2019), https://onlinelibrary.wiley.com/doi/pdf/10.1111/tra.12669.

³P. Gallardo, S. Salas-Pino, and R. R. Daga, Current Genetics **67**, 849 (2021)

the online version of record will be different from this version once it has been copyedited and typeset

PLEASE CITE THIS ARTICLE AS DOI: 10.1063/5.0209119

- ⁴E. Alghoul, J. Basbous, and A. Constantinou, DNA Repair **128**, 103524 (2023).
- ⁵N. Samanta, S. S. Ribeiro, M. Becker, E. Laborie, R. Pollak, S. Timr, F. Sterpone, and S. Ebbinghaus, Journal of the American Chemical Society **143**, 19909 (2021), pMID: 34788540, https://doi.org/10.1021/jacs.1c09589.
- ⁶S. Elbaum-Garfinkle, Y. Kim, K. Szczepaniak, C. C.-H. Chen, C. R. Eckmann, S. Myong, and C. P. Brangwynne, Proceedings of the National Academy of Sciences **112**, 7189 (2015), https://www.pnas.org/doi/pdf/10.1073/pnas.1504822112.
- ⁷L. Jawerth, E. Fischer-Friedrich, S. Saha, J. Wang, T. Franzmann, X. Zhang, J. Sachweh, M. Ruer, M. Ijavi, S. Saha, J. Mahamid, A. A. Hyman, and F. Jülicher, Science **370**, 1317 (2020), https://www.science.org/doi/pdf/10.1126/science.aaw4951.
- ⁸J. A. Morin, S. Wittmann, S. Choubey, A. Klosin, S. Golfier, A. A. Hyman, F. Jülicher, and S. W. Grill, Nature Physics **18**, 271 (2022).
- ⁹R. E. Goldstein and J.-W. van de Meent, Interface Focus **5**, 20150030 (2015), https://royalsocietypublishing.org/doi/pdf/10.1098/rsfs.2015.0030.
- ¹⁰D. Needleman and M. Shelley, Physics Today **72**, 32 (2019).
- ¹¹R. E. Goldstein, J. Fluid Mech. **807**, 1 (2016).
- ¹²R. J. Lasek, J. A. Garner, and S. T. Brady, Journal of Cell Biology **99**, 212s (1984), https://rupress.org/jcb/article-pdf/99/1/212s/1643119/212s.pdf.
- ¹³A. Brown, Journal of Cell Biology **160**, 817 (2003), https://rupress.org/jcb/article-pdf/160/6/817/1521074/jcb1606817.pdf.
- ¹⁴Y. Shen, F. S. Ruggeri, D. Vigolo, A. Kamada, S. Qamar, A. Levin, C. Iserman, S. Alberti, P. S. George-Hyslop, and T. P. J. Knowles, Nature Nanotechnology 15, 841 (2020).
- ¹⁵S. Roy, B. Zhang, V. M.-Y. Lee, and J. Q. Trojanowski, Acta Neuropathologica 109, 5 (2005).
- ¹⁶Y.-C. Liao, M. S. Fernandopulle, G. Wang, H. Choi, L. Hao, C. M. Drerup, R. Patel, S. Qamar, J. Nixon-Abell, Y. Shen, W. Meadows, M. Vendruscolo, T. P. Knowles, M. Nelson, M. A. Czekalska, G. Musteikyte, M. A. Gachechiladze, C. A. Stephens, H. A. Pasolli, L. R. Forrest, P. St George-Hyslop, J. Lippincott-Schwartz, and M. E. Ward, Cell 179, 147 (2019).
- ¹⁷P. P. Gopal, J. J. Nirschl, E. Klinman, and E. L. F. Holzbaurb, Proc. Natl. Ac. Sci. **114**, E2466 (2017).
- ¹⁸S. Timr, S. Melchionna, P. Derreumaux, and F. Sterpone, The Journal of Physical Chemistry B **127**, 3616 (2023), pMID: 37071827, https://doi.org/10.1021/acs.jpcb.3c00253.
- ¹⁹G. Valdes-Garcia, L. Heo, L. J. Lapidus, and M. Feig, Journal of Chemical Theory and Computation 19, 669 (2023), pMID: 36607820, https://doi.org/10.1021/acs.jctc.2c00856.
- ²⁰F. Sterpone, S. Melchionna, P. Tuffery, S. Pasquali, N. Mousseau, T. Cragnolini, Y. Chebaro, J.-F. St-Pierre, M. Kalimeri, A. Barducci, Y. Laurin, A. Tek, M. Baaden, P. H. Nguyen, and P. Derreumaux, Chemical Society Reviews 43, 4871 (2014).
- ²¹S. Timr, D. Gnutt, S. Ebbinghaus, and F. Sterpone, The Journal of Physical Chemistry Letters 11, 4206 (2020), pMID: 32364389, https://doi.org/10.1021/acs.jpclett.0c00699.
- ²²S. Timr and F. Sterpone, The Journal of Physical Chemistry Letters **12**, 1741 (2021), pMID: 33570420, https://doi.org/10.1021/acs.jpclett.0c03626.
- ²³A. Iorio, S. Melchionna, P. Derreumaux, and F. Sterpone, The Journal of Physical Chemistry Letters 15, 1943 (2024), pMID: 38346112, https://doi.org/10.1021/acs.jpclett.3c03084.
- ²⁴R. M. Regy, J. Thompson, Y. C. Kim, and J. Mittal, Protein Science 30, 1371 (2021), https://onlinelibrary.wiley.com/doi/pdf/10.1002/pro.4094.
- ²⁵G. Tesei, T. K. Schulze, R. Crehuet, and K. Lindorff-Larsen, Proceedings of the National Academy of Sciences 118, e2111696118 (2021), https://www.pnas.org/doi/pdf/10.1073/pnas.2111696118.

- ²⁶G. Tesei and K. Lindorff-Larsen, Open Research Europe 2 (2023), 10.12688/openreseurope.14967.2.
- ²⁷G. Valdes-Garcia, K. Gamage, C. Smith, K. Martirosova, M. Feig, and L. J. Lapidus, Cell Reports Physical Science 4, 101415 (2023).
- ²⁸P. Ahlrichs and B. Dünweg, J. Chem. Phys. **111**, 8225 (1999).
- ²⁹F. Sterpone, P. Derreumaux, and S. Melchionna, Journal of Chemical Theory and Computation 11, 1843 (2015), pMID: 26574390, https://doi.org/10.1021/ct501015h.
- ³⁰S. Succi, R. Benzi, A. Calí, and M. Vergassola, "The lattice boltzmann equation: Theory and application," in *Microscopic Simulations of Complex Hydrodynamic Phenomena*, edited by M. Mareschal and B. L. Holian (Springer US, Boston, MA, 1992) pp. 187–203.
- ³¹M. Bernaschi, S. Melchionna, S. Succi, M. Fyta, E. Kaxiras, and J. Sircar, Computer Physics Communications 180, 1495 (2009).
- ³²M. Chiricotto, S. Melchionna, P. Derreumaux, and F. Sterpone, The Journal of Chemical Physics **145**, 035102 (2016), https://doi.org/10.1063/1.4958323.
- ³³M. Chiricotto, S. Melchionna, P. Derreumaux, and F. Sterpone, The Journal of Physical Chemistry Letters 10, 1594 (2019), https://doi.org/10.1021/acs.jpclett.9b00423.
- ³⁴F. Sterpone, P. Derreumaux, and S. Melchionna, J. Phys. Chem. B 12, 1573–1579 (2018).
- ³⁵O. Languin-Cattoën, E. Laborie, D. O. Yurkova, S. Melchionna, P. Derreumaux, A. V. Belyaev, and F. Sterpone, Polymers 13 (2021), 10.3390/polym13223912.
- ³⁶E. Laborie, S. Melchionna, and F. Sterpone, The Journal of Chemical Physics 158, 095103 (2023), https://pubs.aip.org/aip/jcp/article-pdf/doi/10.1063/5.0135216/16792191/095103_1_online.pdf.
- ³⁷J. A. Izaguirre, C. R. Sweet, and V. S. Pande, "Multiscale dynamics of macromolecules using normal mode Langevin," in *Biocomputing 2010* (World Scienctific, 2010) pp. 240–251.
- ³⁸E. Guyon, J.-P. Hulin, L. Petit, and C. D. Mitescu, *Physical Hydrodynamics* (Oxford University Press, 2015).
- ³⁹S. A. McBride, S. P. Sanford, J. M. Lopez, and A. H. Hirsa, Soft Matter 12, 3461 (2016).
- ⁴⁰P. Eastman, J. Swails, J. D. Chodera, R. T. McGibbon, Y. Zhao, K. A. Beauchamp, L.-P. Wang, A. C. Simmonett, M. P. Harrigan, C. D. Stern, R. P. Wiewiora, B. R. Brooks, and V. S. Pande, PLOS Computational Biology 13, 1 (2017).
- ⁴¹A. Alexander-Katz and R. R. Netz, Macromolecules **41**, 3363 (2008).
- ⁴²J. Jaspe and S. J. Hagen, Biophys. J. **91**, 3415 (2006).
- ⁴³ A. Ortega, D. Amorós, and J. García de la Torre, Biophysical Journal **101**, 892 (2011)
- ⁴⁴Y. Wang, C. Li, and G. J. Pielak, Journal of the American Chemical Society 132, 9392 (2010), pMID: 20560582, https://doi.org/10.1021/ja102296k.
- ⁴⁵S. R. McGuffee and A. H. Elcock, PLOS Computational Biology 6, 1 (2010).
- ⁴⁶M. H. G. Duits, S. Ghosh, and F. Mugele, Langmuir **31**, 5689 (2015), pMID: 25965857, https://doi.org/10.1021/acs.langmuir.5b01369.
- ⁴⁷S. Ghosh, F. Mugele, and M. H. G. Duits, Physical Review E **91**, 052305 (2015).
- ⁴⁸J. M. Rallison, Annual Review of Fluid Mechanics **16**, 45 (1984), https://doi.org/10.1146/annurev.fl.16.010184.000401.
- 49A New Algorithm for Contact Angle Estimation in Molecular Dynamics Simulations, International Conference on Nanochannels, Microchannels, and Minichannels, Vol. ASME 2015 13th International Conference on Nanochannels, Microchannels, and Minichannels (2015) https://asmedigitalcollection.asme.org/ICNMM/proceedings-pdf/ICNMM2015/56871/V001T04A007/4247094/v001t04a007-
- icnmm2015-48569.pdf. ⁵⁰G. Danker, P. M. Vlahovska, , and C. Misbah, Phys. Rev. Lett. **102**, 148102 (2000)